JOURNAL OF COMPUTATIONAL PHYSICS **133,** 193–204 (1997)
ARTICLE NO. CP975673

A Robust Low Diffusive Kinetic Scheme for the Navier–Stokes/Euler Equations

Jean-Marc Moschetta* and D. I. Pullin†

*École Nationale Supérieure de l'Aéronautique et de l'Espace, 31400 Toulouse, France; †Graduate Aeronautical Laboratories, California Institute of Technology, California 91125
E-mail: moscheta@supaero.fr; dip@galcit.caltech.edu

Received October 25, 1995; revised February 20, 1997

A new kinetic scheme based on the equilibrium flux method (EFM) and modified using Osher intermediate states is proposed. This new scheme called EFMO combines the robustness of the equilibrium flux method and the accuracy of flux-difference splitting schemes. The original EFM scheme is expressed in terms of simple wave decomposition in which only the linearly degenerate subpath is calculated from Osher numerical flux while nonlinear waves are still evaluated from the regular EFM splitting. Owing to its capability of withstanding intense nonlinear waves and yet exactly resolving contact discontinuities, EFMO is particularly well suited for the resolution of the Navier–Stokes equations as demonstrated by a series of severe test cases including the high-speed viscous flow around a cone, a shock-boundary layer interaction problem, a vacuum apparition problem, the hypersonic flow around a circular cylinder at Mach 100, and the forward-facing step at Mach 3.

1. INTRODUCTION

Maximizing both robustness and accuracy is a primary goal for designing numerical schemes suitable for practical applications in gas dynamics problems. This requirement is especially important for the resolution of the full Navier–Stokes equations in the hypervelocity regime where intense shock waves and boundary layers are simultaneously present.

Among the various upwind shock-capturing schemes developed in the 1980s, kinetic schemes such as the equilibrium flux method (EFM) developed by Pullin [1] have proved to be among the most robust algorithms and therefore especially well suited for the numerical simulation of high-speed flows around bodies [2, 3].

EFM is based on the observation that the Euler equations are moments of the Boltzmann equation. An analytical expression for the flux of mass, momentum, and energy at each cell interface can be derived [4] from the assumption that the velocity distribution within each cell remains Maxwellian during a sufficiently short period of time. Updated values for the conservative quantities are obtained from the discretized Euler equations written in conservation law form. A unique Maxwellian distribution is then constructed from the updated physical values of each cell and the process repeats.

Among its mathematical properties, EFM has been formally shown to be entropy satisfying [5] and positivity preserving [6]. Furthermore, Macrossan [7] has pointed out the upwinding mechanism of EFM by proving that its numerical dissipation vanishes when the Mach number increases. For moderate values of the Mach number, however, EFM suffers from an excessive numerical diffusion that can dramatically smear out contact discontinuities.

An alternative approach developed independently by Macrossan [8] and Xu [9] consists of directly reconstructing the conservative variables at the interface from the contribution of two half-Maxwellians associated with the physical states on either sides of the interface. The resulting scheme is very low diffusive and performs well for boundary layer flows but at the same time poorly withstands even moderate shock waves.

Further improvements have been made recently by Prendergast and Xu [10–12] in an interesting effort to take into account the collision phase of the Boltzmann process on the basis of the BGK model. In this fairly complex approach, accurate results are obtained in a wide variety of test cases at the price of the use of a tunable parameter used to define the collision time.

The starting point of this paper is the observation that EFM belongs to the large family of flux-vector splitting schemes (FVS). Indeed, FVS schemes such as Van Leer (VL) or Steger–Warming (SW) splittings share with EFM a comparable robustness in the capture of intense shocks and rarefaction waves although typical sonic pressure kinks associated with VL and SW schemes do not show up with EFM. FVS methods are also computationally inexpensive and easy to use in implicit schemes. However, FVS schemes have lost much of their appeal with the rise of Navier–Stokes solvers since they ignore linear waves (i.e., contact discontinuities). This leads to excessive numerical diffusion and the artificial broadening of boundary layers that cannot be simply cured by using high-order differencing [13].

0021-9991/97 $25.00

Subsequently, efforts have been made to improve FVS schemes in the field of viscous flow prediction. Following the idea of Hänel *et al.* [14], Van Leer drastically improved his original scheme by introducing an extrapolation on the tangential momentum and the total enthalpy as an attempt to reintroduce the flux-difference splitting approach (FDS) [15]. Unfortunately, the resulting Van Leer/Hänel scheme leads to unphysical pressure glitches at the edge of the boundary layer. Other methods such as AUSM have been suggested [16, 17] in order to reduce the numerical diffusion of FVS schemes but these methods generally lead to marginally stable schemes and additional fixes are necessary to damp some pressure oscillations in the vicinity of shocks [18].

On the other hand, FDS schemes such as Roe or Osher schemes have proved to be very accurate for viscous flow calculations since they exactly capture stationary contact discontinuities. A problem with the FDS methods is that they often require intricate corrections to enhance stability in the capture of intense nonlinear waves. For the Roe scheme, several corrections have been proposed to guarantee the correct entropy production across shocks and to cure postshock oscillations and other reported pathological behaviour such as the ''carbuncle phenomenon'' or the ''kinked Mach stem'' as discussed by Quirk [19]. Such corrections generally introduce a significant amount of artificial diffusion which degrades the ability of FDS schemes to accurately compute boundary layers [20].

The motivation of the present work is to combine the robustness of FVS methods for strong shocks with the accuracy of FDS methods for contact discontinuities. Following Coquel [21], we propose to replace the highly diffusive resolution of contact discontinuities resulting from the original formulation of EFM by the exact resolution of contact discontinuities provided by Osher's scheme. The resulting scheme EFMO combines the desirable properties of each of the FVS and FDS approaches, i.e., robustness for nonlinear waves and accuracy for linear waves.

2. ANALYSIS

As a member of the FVS scheme family, EFM suffers from excessive diffusion in the resolution of contact discontinuities. This can be easily understood by considering the net transverse momentum flux across a contact discontinuity (L denotes the left state, R right state)

$$\begin{aligned} F^{\text{net}}_{\text{mom}} &= F^{+}_{\text{mass}} v_{pR} + F^{-}_{\text{mass}} v_{pL}, \\ &= F^{+}_{\text{mass}} (v_{pR} - v_{pL}), \end{aligned} \tag{1}$$

where v_{pR} and v_{pL} are the tangential components of the velocity on either sides of the contact discontinuity. The presence of a nonvanishing transverse momentum can be interpreted as an equivalent numerical viscous stress with a corresponding numerical viscosity coefficient proportional to the cell size as calculated by Macrossan [7]. A similar analysis can be made for a temperature gradient and would lead to a numerical heat conductivity.

In both cases, this analysis shows that the application of EFM as well as the use of any FVS method for the resolution of the Navier–Stokes equations can lead to inaccurate results if the grid is not sufficiently refined in the regions of the flow where the effects of the natural viscosity are significant. A noticeable improvement for EFM can be obtained by applying an intuitive idea suggested by Hänel [14] for Van Leer splitting. It consists of replacing the expression for the net transverse momentum by one borrowed from the FDS approach,

$$F^{\text{net}}_{\text{mom}} = F^{\text{net}}_{\text{mass}} \cdot v^{*}_{p}, \tag{2}$$

where

$$v^{*}_{p} = \begin{cases} v_{pL} & \text{if } F^{\text{net}}_{\text{mass}} > 0 \\ v_{pR} & \text{otherwise.} \end{cases} \tag{3}$$

A similar formula can be applied to the energy flux in order to remove the undesirable numerical heat conductivity. The original formulation of the EFM energy flux can then be replaced by

$$F^{\pm}_{\text{eng}} = F^{\pm}_{\text{mass}} \cdot H, \tag{4}$$

where H is the specific total enthalpy for the cell considered as suggested by Hänel for Van Leer's scheme [22]. Thus, a similar extrapolation for the energy flux can be applied,

$$F^{\text{net}}_{\text{eng}} = F^{\text{net}}_{\text{mass}} \cdot H^{*}, \tag{5}$$

where

$$H^{*} = \begin{cases} H_L & \text{if } F^{\text{net}}_{\text{mass}} > 0 \\ H_R & \text{otherwise.} \end{cases} \tag{6}$$

In the following, we refer to the resulting modified EFM scheme as EFMT. Although the EFMT shares with EFM the same robustness for the capture of intense shock waves and an improved accuracy for the calculation of boundary layers, this simple variant leads to a pressure glitch at the edge of the boundary layer, as is shown in the next section.

A more promising approach consists of further blending the FVS and the FDS methods in a more rigorous way based on the simple wave approach used in Osher's scheme. The EFMO scheme (EFM and Osher) is based

on a formal similarity between the mathematical expressions of the EFM numerical flux and the Osher numerical flux.

In Osher's method [23], the numerical flux is given by

$$F_O(U_L, U_R) = \tfrac{1}{2}\left[F_L + F_R - \int_{LN} |A| dw - \int_{NL} |A| dw \right], \quad (7)$$

where LN refers to the linearly degenerated subpath which corresponds physically to a contact discontinuity, and NL refers to the genuinely nonlinear subpaths which correspond to either compression or rarefaction waves.

The matrix $|A|$ is the absolute value of the Jacobian matrix of the exact flux F and is defined in the sense

$$|A| = R|\Lambda|R^{-1}, \quad |\Lambda| = \mathrm{Diag}(|\lambda_p|)_{p=1,\dots m}, \quad (8)$$

where λ_p is an eigenvalue of A.

The EFM numerical flux [1] defined as

$$F_{\mathrm{EFM}}(U_L, U_R) = F^+(U_L) + F^-(U_R) \quad (9)$$

can be put in a form similar to Osher's numerical flux,

$$F_{\mathrm{EFM}}(U_L, U_R) = \tfrac{1}{2}\left[F_L + F_R - \int_{LN} |B| dw - \int_{NL} |B| dw \right], \quad (10)$$

where $|B|$ is now defined as $|B| = B^+ - B^-$ and $B^\pm$ is the Jacobian matrix of the fluxes $F^\pm$.

The main idea, following the hybrid upwind splitting (HUS) of Coquel [21], is to retain the integral corresponding to the nonlinear path (shock wave) in the EFM numerical flux and to replace the integral corresponding to the linear path (contact discontinuity) by the one taken from Osher's numerical flux. The resulting numerical flux is then

$$F_{\mathrm{EFMO}}(U_L, U_R) = \tfrac{1}{2}\left[F_L + F_R - \int_{LN} |A| dw - \int_{NL} |B| dw \right], \quad (11)$$

or equivalently,

$$F_{\mathrm{EFMO}}(U_L, U_R) = F_{\mathrm{EFM}}(U_L, U_R) + \tfrac{1}{2}\int_{LN} (|B| - |A|) dw, \quad (12)$$

where the integral represents an antidiffusive flux which almost vanishes in the vicinity of shocks and removes the excessive numerical dissipation near contact discontinuities.

The previous relation can be further simplified by defining two intermediate states, U_1 and U_2, determined by using Riemann invariants in the sense of Lax as implied in the original Osher's method. In the case of a calorically perfect gas, U_1 and U_2 are determined by solving the following problems:

nonlinear subpath (L)–(1),

$$\frac{p_L}{\rho_L^\gamma} = \frac{p_1}{\rho_1^\gamma}, \quad (13)$$

$$v_{nL} + \frac{2\varepsilon}{\gamma - 1} a_L = v_{n1} + \frac{2\varepsilon}{\gamma - 1} a_1, \quad (14)$$

$$v_{pL} = v_{p1}, \quad v_{qL} = v_{q1}. \quad (15)$$

linear subpath (1)–(2),

$$v_{n1} = v_{n2} = v_n^*, \quad (16)$$

$$p_1 = p_2 = p^*. \quad (17)$$

nonlinear subpath (2)–(R)

$$\frac{p_2}{\rho_2^\gamma} = \frac{p_R}{\rho_R^\gamma}, \quad (18)$$

$$v_{n2} - \frac{2\varepsilon}{\gamma - 1} a_2 = v_{nR} - \frac{2\varepsilon}{\gamma - 1} a_R, \quad (19)$$

$$v_{p2} = v_{pR}, \quad v_{q2} = v_{qR}, \quad (20)$$

where p, ρ, a are respectively the pressure, density, and sound speed and v_n, v_p, v_q are the components of the velocity in a local system of axis in which v_n is the component of the velocity normal to the interface and v_p, v_q are the two other components of the velocity tangential to the interface.

In the above relations, $\varepsilon = +1$ and $\varepsilon = -1$ for paths in the natural order and reverse order, respectively. Numerical experiments have shown that the natural order is preferable to the reverse order originally proposed by Osher because it avoids the carbuncle phenomenon in some situations. However, this conclusion might well be different for a different category of problems [24].

The two intermediate states are then used to calculate the antidiffusive flux so that eventually the EFMO numerical flux reads

$$F_{\mathrm{EFMO}}(U_L, U_R) = F_{\mathrm{EFM}}(U_L, U_R) + \begin{cases} -F^-(U_2) + F^-(U_1) & \text{if } v_n^* > 0 \\ +F^+(U_2) - F^+(U_1) & \text{otherwise,} \end{cases} \quad (21)$$

where v_n^* is the common value of the normal velocity component for both intermediate states and $F^{\pm}$ are the regular EFM fluxes which appear in Eq. (9).

In addition to the mathematical description of the present method, the following properties of EFMO should be noted:

1. the sound speed of the nonlinear wave does not play any role as in Osher's scheme in this approach and only one switch based on the normal velocity is needed to implement EFMO starting from an existing EFM scheme;

2. the existence of two intermediate states (U_1, U_2) is not always guaranteed for any set of left and right states (U_L, U_R). Should this occur, the antidiffusive flux is set to zero and the method reverts to regular EFM. This situation only arises for extreme initial conditions such as the vacuum apparition problem presented in the next section and is limited to the very first time steps of the calculation;

3. from the expression of the EFMO numerical flux, it is clear that in the case of a pure discontinuity of tangential velocity, the transverse momentum flux reduces to zero as in the case of EFMT.

Viscous terms are computed using a second-order accurate central differencing with a viscosity governed by Sutherland's law. When viscous terms are included, the equations are full Navier–Stokes. Finally, second-order accuracy in space is achieved by using a standard MUSCL reconstruction of the primitive variables with the *minmod* slope limiter. In the following, some results will be presented as ''second order'' or ''first-order accurate'' referring to an accuracy in space only. In all cases, only first-order accuracy in time is achieved.

3. RESULTS AND DISCUSSION

Five sets of problems were used to evaluate the performance of the new algorithm. First there is the quasi 2D viscous conical flow patterned after the experiments of Van Leer [13]. The second test case is the interaction of an oblique shock wave with a laminar boundary layer studied experimentally by Hakkinen *et al.* [25]. The third set involves 1D inviscid ''vacuum apparition'' problems inspired from Sjögreen test cases [26]. The fourth test case deals with the hypersonic flow over a circular cylinder at Mach 100. Finally, the fifth problem is a Mach 3 wind tunnel with a forward-facing step as introduced by Emery and described by Woodward and Collela [27].

Case 1. This test case provides an ideal benchmark for testing the accuracy of a numerical scheme for viscous calculations. A 10° half-angle cone at 0° angle of attack is considered with a conical computational domain spanning 5° out from the surface of the cone using 50 cells equally spaced. The freestream Mach number is 7.95, the Reynolds number is 4.2×10^5, and the static temperature 55.4 K. An adiabatic wall is assumed with a Prandtl number of 1.0 in order to compare the present method to the analytical solution [28],

$$T_{\text{wall}} = T_\infty \left(1 + \frac{\gamma - 1}{2} M_\infty^2\right), \tag{22}$$

with $\gamma = 1.4$. We present first-order accurate results by using a 3D code with a ''stepback'' mode which consists of imposing freestream conditions at the input plane for the first time step and setting the inflow conditions for the following time steps equal to the outflow plane. After convergence of the process, both inflow and outflow planes are identical and we obtain a quasi-conical solution of the Navier–Stokes equations.

With the regular EFM scheme, the boundary layer is broadened if compared with the EFMT and EFMO solutions as seen in Fig. 1a on the temperature profile. Close analysis of Fig. 1a reveals that the wall temperature obtained by EFM is significantly far from the theoretical value correctly predicted by EFMT and EFMO . Furthermore, an unphysical pressure glitch is clearly visible on the pressure profile (Fig. 1b) at the edge of the boundary layer for the EFMT solution while this pressure glitch is absent from the EFMO solution.

Case 2. The second test case is a 2D viscous flow which consists of the interaction of an oblique shock wave with a laminar boundary layer. The impinging oblique shock incident upon the boundary layer on the flat plate is chosen to be strong enough to cause the boundary layer to separate from the surface and reattach downstream. The problem has been studied experimentally by Hakkinen *et al.* [25] at the following freestream conditions: $M_\infty = 2.0$ – $\text{Re}_\infty = 2.96 \times 10^5$, and the incident shock wave is imposed such that the shock intersects the flat plate at 32.6°. The Reynolds number is based on the reference length L_{ref}, measured from the leading edge to the interaction point.

The computational results were obtained using a 50×50 grid above the plate surface. The grid points were uniformly spaced in the x direction and exponentially stretched in the y direction in such a way that the first cell by the wall has a constant height of $\Delta y/L_{\text{ref}} = 10^{-3}$. Approximately 15 points spanned the boundary layer.

The skin friction coefficient defined by $Cf = \tau/(\rho_\infty u_\infty^2/2)$ along the flat plate is shown in Fig. 2. Second-order accurate results obtained by EFM and EFMO are compared with the experimental results of Hakkinen *et al.* [25]. The experimental probes in the separated region were unable to measure skin friction other than to show that it was zero or negative. The numerical results obtained with EFMO are very consistent with experimental data. The skin friction of the EFMO scheme behind the separation

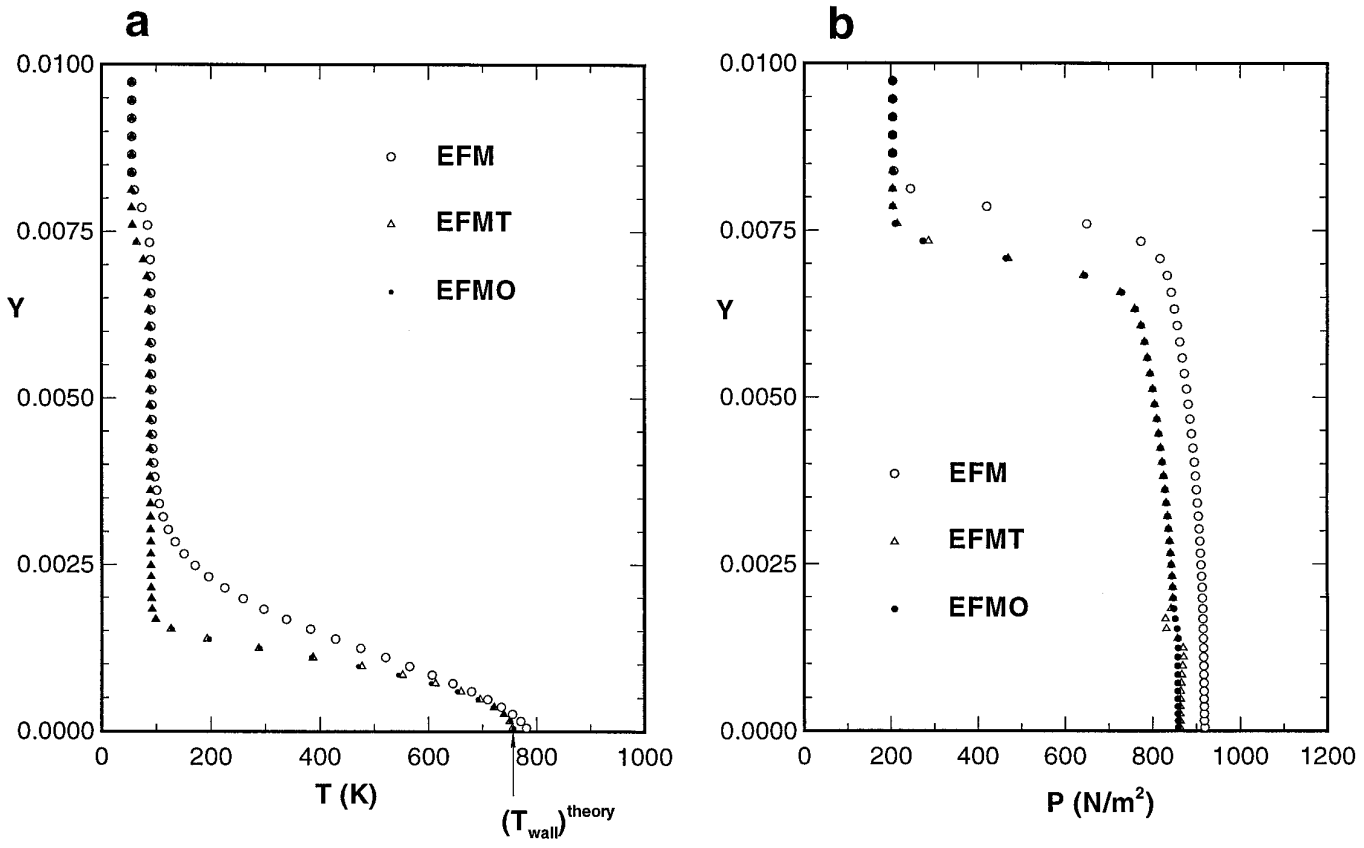

FIG. 1. Hypersonic conical flow – $M_\infty = 7.95$, Re $= 4.2 \times 10^5$, Pr $= 1.0$; first-order accurate results: (a) temperature profile; (b) pressure profile using EFM, EFMT, and EFMO.

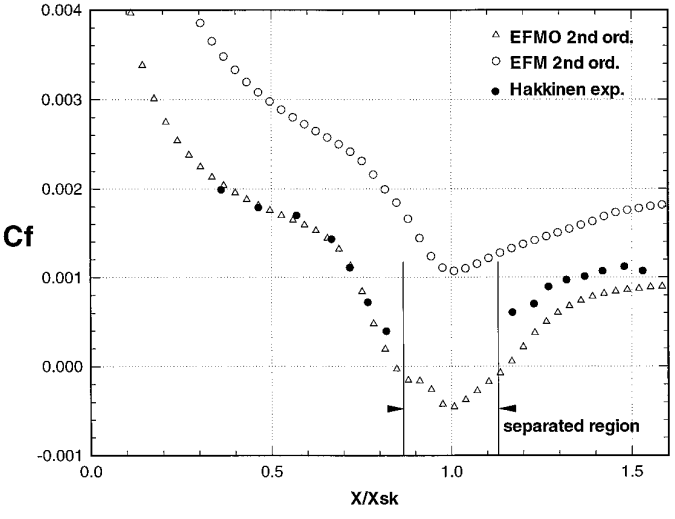

FIG. 2. Case 2. $M_\infty = 2.0$ – $\mathrm{Re}_\infty = 2.96 \times 10^5$ skin friction coefficient along plate surface for shock/boundary layer interaction flow.

region is lower than that of the experiment, which is also predicted by other computational results [29–32]. On the other hand, the skin friction coefficient predicted by EFM using the same grid is much higher and the calculation misses the separation of the boundary layer (*Cf* remains strictly positive). Although the mesh is still fairly coarse, it is interesting to see that EFMO provides a satisfactory answer to the problem if compared with experimental data while EFM fails to predict separation. However, both EFM and EFMO solutions should eventually converge toward a unique answer if the grid was further refined.

Case 3. A vacuum apparition problem is considered here to assess the robustness of the present method near low densities. This 1D inviscid problem consists of starting from the initial velocity distribution,

$$u(x) = \begin{cases} u_L = -u_0, & x < x_0, \\ u_R = +u_0, & x \geq x_0, \end{cases} \tag{23}$$

a uniform temperature T_0, and density ρ_0 with $\gamma = 1.4$. A straightforward analysis based on the theory of characteris-

tics shows that this Riemann problem can have two types of solutions depending on the value of the Mach number,

$$M_0 = u_0/a_0, \tag{24}$$

where a_0 is the initial sound speed of the gas.

(a) $0 < M_0 < 2/(\gamma - 1)$. The solution consists of two rarefaction waves travelling in opposite directions and one contact discontinuity that stays at rest at $x = x_0$. A constant-pressure region (V) appears between the interior limits of the rarefaction waves in which the state of the gas is totally defined by

$$\begin{aligned} u_V &= 0 \\ a_V &= a_0\left(1 - \frac{\gamma - 1}{2} M_0\right) \\ p_V &= p_0\left(1 - \frac{\gamma - 1}{2} M_0\right)^{2\gamma/(\gamma-1)} \end{aligned} \tag{25}$$

for any (x, t) such that

$$\frac{\gamma - 1}{2} u_0 - a_0 \le \frac{x - x_0}{t} \le a_0 - \frac{\gamma - 1}{2} u_0. \tag{26}$$

In this case, it is important to note that the actual value of the pressure p_V between the two rarefaction waves is positive. Therefore, there is no vacuum apparition, strictly speaking.

(b) $M_0 \ge 2/(\gamma - 1)$. In this case, the difference in velocity becomes so strong that a real zero-pressure region takes place. The solution to the Riemann problem consists of two rarefaction waves travelling in opposite directions followed by two contact discontinuities. Vacuum appears between these two contact discontinuities, where

$$\begin{aligned} u_V &= 0 \\ a_V &= 0 \\ p_V &= 0 \end{aligned} \tag{27}$$

for any (x, t) such that

$$\frac{2a_0}{\gamma - 1} - u_0 \le \frac{x - x_0}{t} \le u_0 - \frac{2a_0}{\gamma - 1}. \tag{28}$$

In this second case, the velocity distribution is discontinuous across the limits of the vacuum region.

Note that in both Sjögreen ''vacuum apparition'' problems only the first situation ($M_0 < 5$) was considered [26]. This is simply because strict positivity of pressure and density is required to mathematically guarantee the positivity preserving property of a Riemann solver. It is nonetheless interesting to try to simulate a real vacuum apparition problem as a more severe benchmark for robustness. In the following, two sets of initial conditions corresponding to cases (a) and (b), respectively, are considered to evaluate the robustness of our method. In both cases, the initial temperature is $T_0 = 300$ K and the initial density is $\rho_0 = 1$ kg/m^3.

Test case (3*a*),

$$u_0 = 1000 \text{ m/s}, \tag{29}$$

which corresponds to $M_0 = 2.88 < 5$ (near vacuum condition).

Test case (3*b*),

$$u_0 = 2000 \text{ m/s}, \tag{30}$$

which corresponds to $M_0 = 5.76 > 5$ (real vacuum).

A uniform grid with 100 points is used in all calculations to cover the computational domain [0; 1] with $x_0 = 0.5$. First- and second-order accurate results are shown on Fig. 3 for Test case (3a) using EFMO. Pressure and density distributions are shown on a logarithmic scale to better appreciate the relative error of the numerical results in the near vacuum region. It has been a common practice to plot the energy profile for this problem. However, because the temperature is defined here as the ratio of two vanishing quantities, we believe that it provides a much more sensitive indication of the accuracy of the numerical results. In particular, it is interesting to note the sudden peak in temperature in the vicinity of the stationary contact discontinuity. This pathological behaviour has been recently pointed out by Toro [33] for all conservative methods. Also, Fig. 3 shows that for this test case, the second-order solution is a little closer to the analytical solution while the robustness of the algorithm is not affected.

For test case (3b), we present first-order accurate results obtained with EFMO and the HLLE–Riemann solver [34] (Fig. 4). Again, the logarithmic axis is used for the pressure and the density distribution to see details that would not be visible with a usual linear axis. Because of its enormous numerical diffusion, HLLE produces poor results in the near vacuum region where the predicted density does not drop below 5×10^{-3}kg/m^3 while EFMO predicts a density as low as 2×10^{-8}kg/m^3 (and even lower with a second-order reconstruction). The discrepancy between the two methods is evident on the temperature distribution. The velocity distribution is very difficult to correctly simulate because of its vertical slopes followed by a horizontal pro-

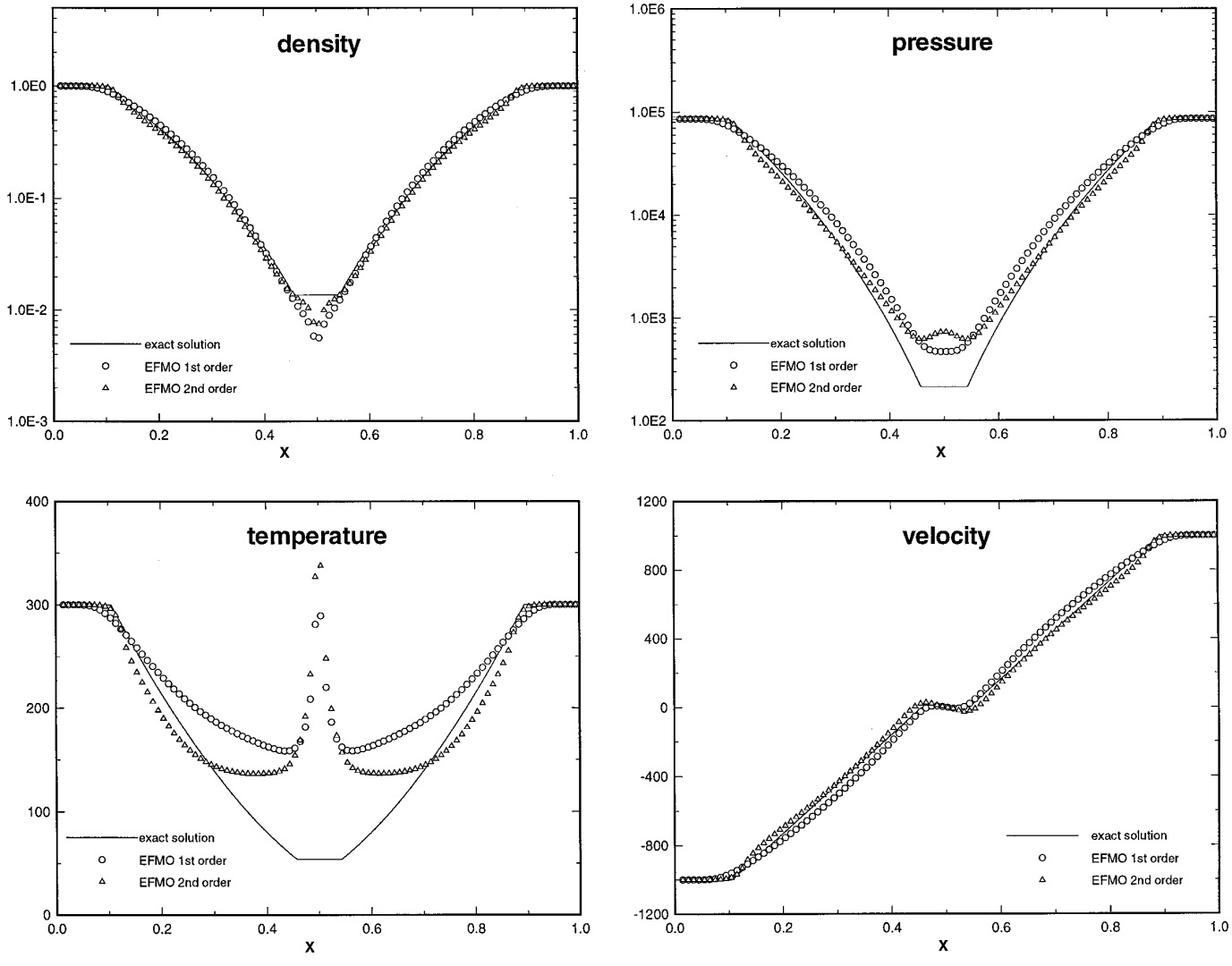

FIG. 3. Case 3a. $M_R = -M_L = 2.88$ first- and second-order accurate results with EFMO.

file. Neither HLLE nor EFMO resolves this structure adequately with the present grid resolution.

It should be acknowledged that the third test case presented here is not self-consistent physically, owing to the very low density level that would require a rarefied gas model. However, it is most challenging numerically since it is a very extreme situation for which most approximate Riemann solvers would simply blow up (such as Roe scheme among others).

Finally, let us stress that in the two vacuum apparition problems presented above, EFM results are very comparable to EFMO results. This is not surprising since strong rarefaction waves are nonlinear waves and are still handled by the regular EFM part. Therefore, EFMO clearly retains the robustness of EFM in this case.

Case 4. The fourth test case is aimed at evaluating the robustness of the present method in the presence of extremely intense shock waves. This 2D inviscid problem consists of an initially uniform flow impinging on a circular cylinder at Mach 100. The freestream conditions are defined as

$$\rho = 1.0\,\mathrm{kg/m^3}, \quad u = 34719\,\mathrm{m/s}, \quad T = 300\,\mathrm{K} \qquad (31)$$

with $\gamma = 1.4$. A grid of 50×50 cells is used to compute the solution with EFM and EFMO at second-order accuracy. The outer limit of the domain is an ellipse which center is located at a distance of one radius downstream and which semi-axis are equal to 1.6 and 2.8 radii, respectively. A stretching factor of 1.1 is applied in the direction normal to the wall while uniform spacing is applied in the direction tangent to the wall. Initially, the computational

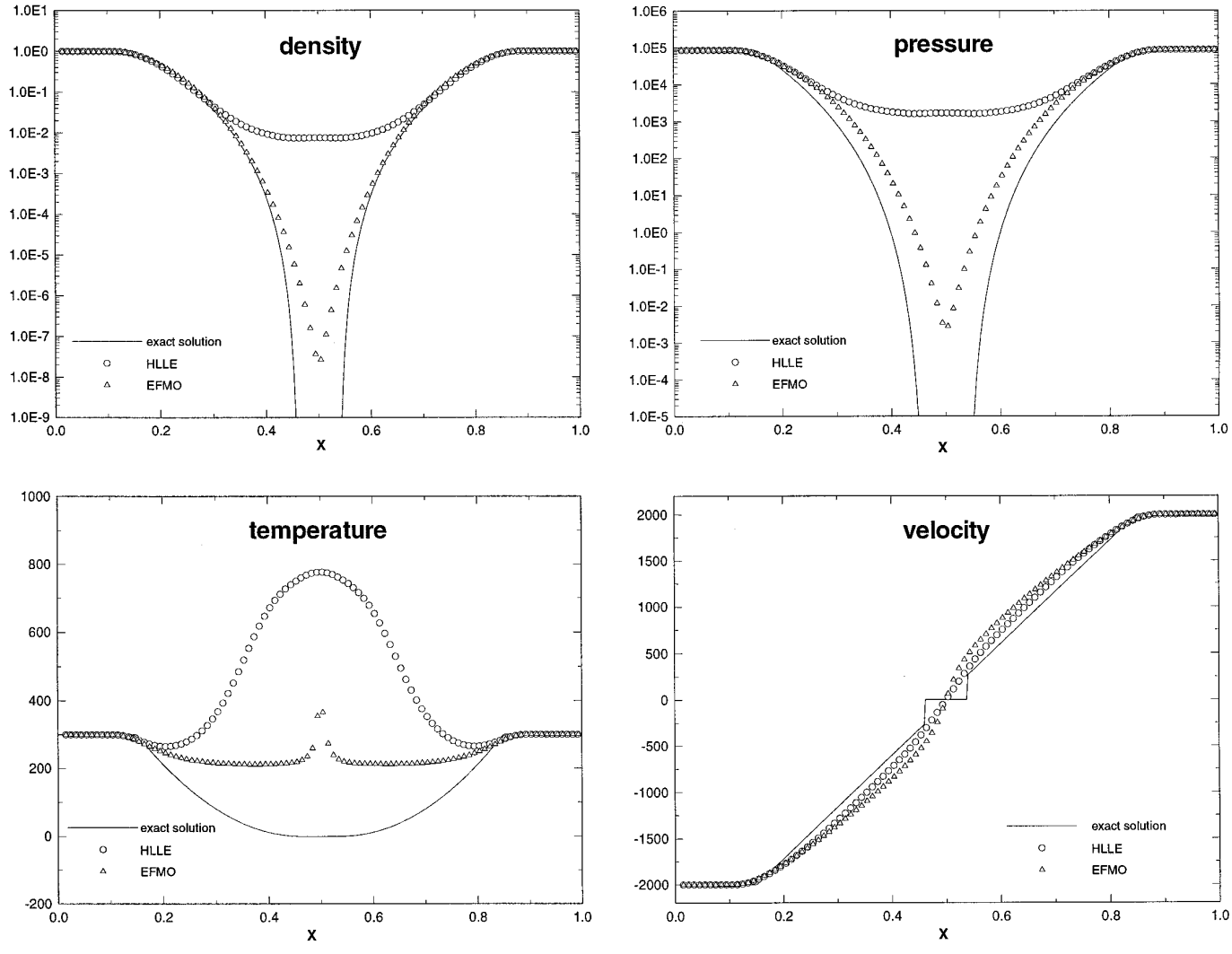

FIG. 4. Case 3b. $M_R = -M_L = 5.76$ first-order accurate results with HLLE and EFMO.

domain is filled with a uniform flow corresponding to the freestream conditions and the governing equations are integrated in time with a CFL = 0.9 until a steady state is reached.

While most FDS schemes fail to give an answer to this problem owing to the very steep pressure gradient across the bow shock, very close agreement is obtained for the EFM and EFMO solutions in terms of pressure contours (see Fig. 5). No carbuncle phenomenon is observed along the stagnation line and in both cases, the shock standoff distance is very close to the theoretical value for high Mach numbers [35],

$$\frac{\Delta}{R} = 0.386, \tag{32}$$

where R is the radius of the cylinder. On the temperature contours, a slight glitch, limited to the near wall region, is visible only with EFMO. In viscous calculations, this glitch is damped by the natural viscosity (see the results on the viscous cone). It is not clear at that point whether this flaw is of the same origin as Noh's effect [36] which can be observed more or less clearly for any shock-capturing scheme or if it is due to a lack of dissipation in a region where the normal velocity is very small. Further investigation is certainly needed here.

Case 5. As a last test case that gathers all the main features of the four previous test cases, we present here the results obtained with EFM and EFMO for the forward-facing step in a wind tunnel at Mach 3 [27]. This unsteady inviscid 2D problem is defined by the following freestream and initial conditions:

$$\rho = 1.0\ \text{kg/m}^3, \quad u = 1041.6\ \text{m/s}, \quad T = 300\ \text{K}. \tag{33}$$

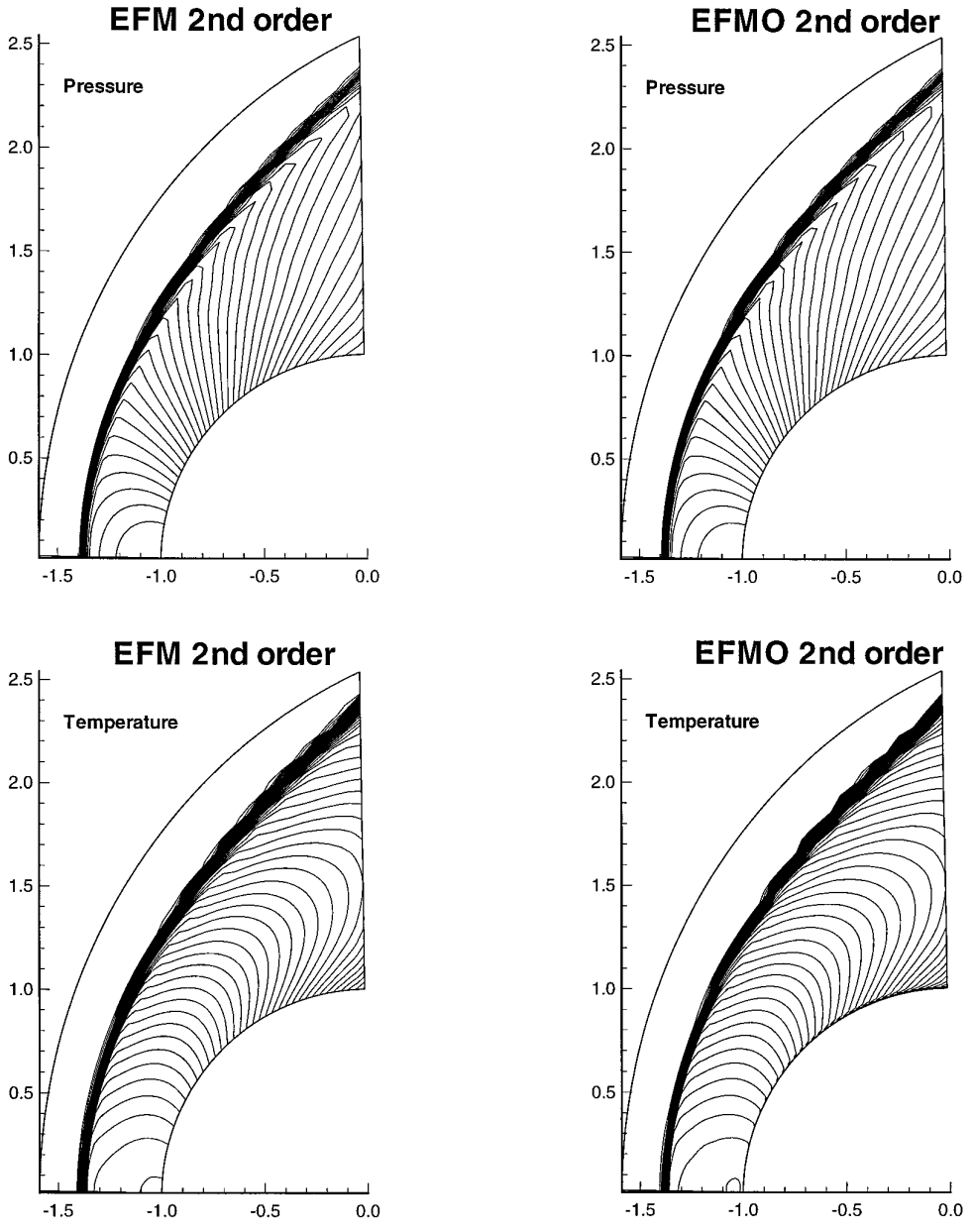

FIG. 5. Hypersonic flow past a circular cylinder—$M_\infty = 100$—second-order accurate results with EFM and EFMO; pressure and temperature contours.

A 240×80 nonuniform cartesian grid is used. Because of the presence of a geometrical singularity local refinement is performed in a region surrounding the corner as shown in Fig. 6. The computational domain is 1 m wide and 3 m long and the step is 0.2 m high and is located 0.6 m from the inflow section. The time at which the solution is presented is $t = 8.64 \times 10^{-3}$ s, which corresponds to a dimensionless time of 3.0 in Woodward and Colella unit system. At this specific value of t, many complex features are present in the flowfield including a detached bow shock with a Mach stem on the upper wall giving rise to a contact discontinuity and a reflected oblique shock hitting the lower wall. A particularly interesting region is the region surrounding the corner where a very strong expansion takes place, the gas being accelerated from subsonic to supersonic speed. On Fig. 7, density and pressure contours are presented in order to see all the different physical features mentioned so far. In both pictures, a Mach stem is visible near the upper wall and an oblique shock is reflected toward the upper side of the step and then upward

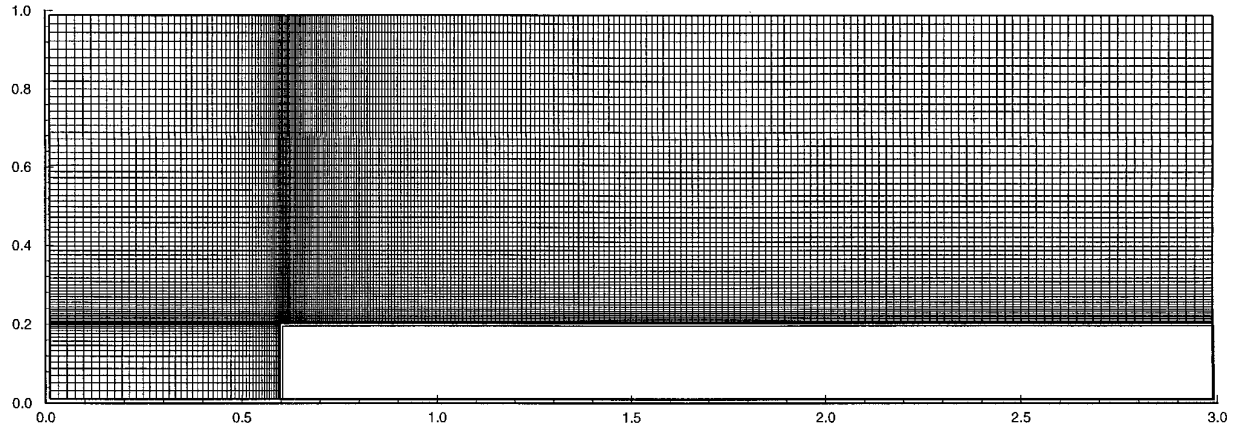

FIG. 6. 240 × 40 refined grid for the forward-facing step problem.

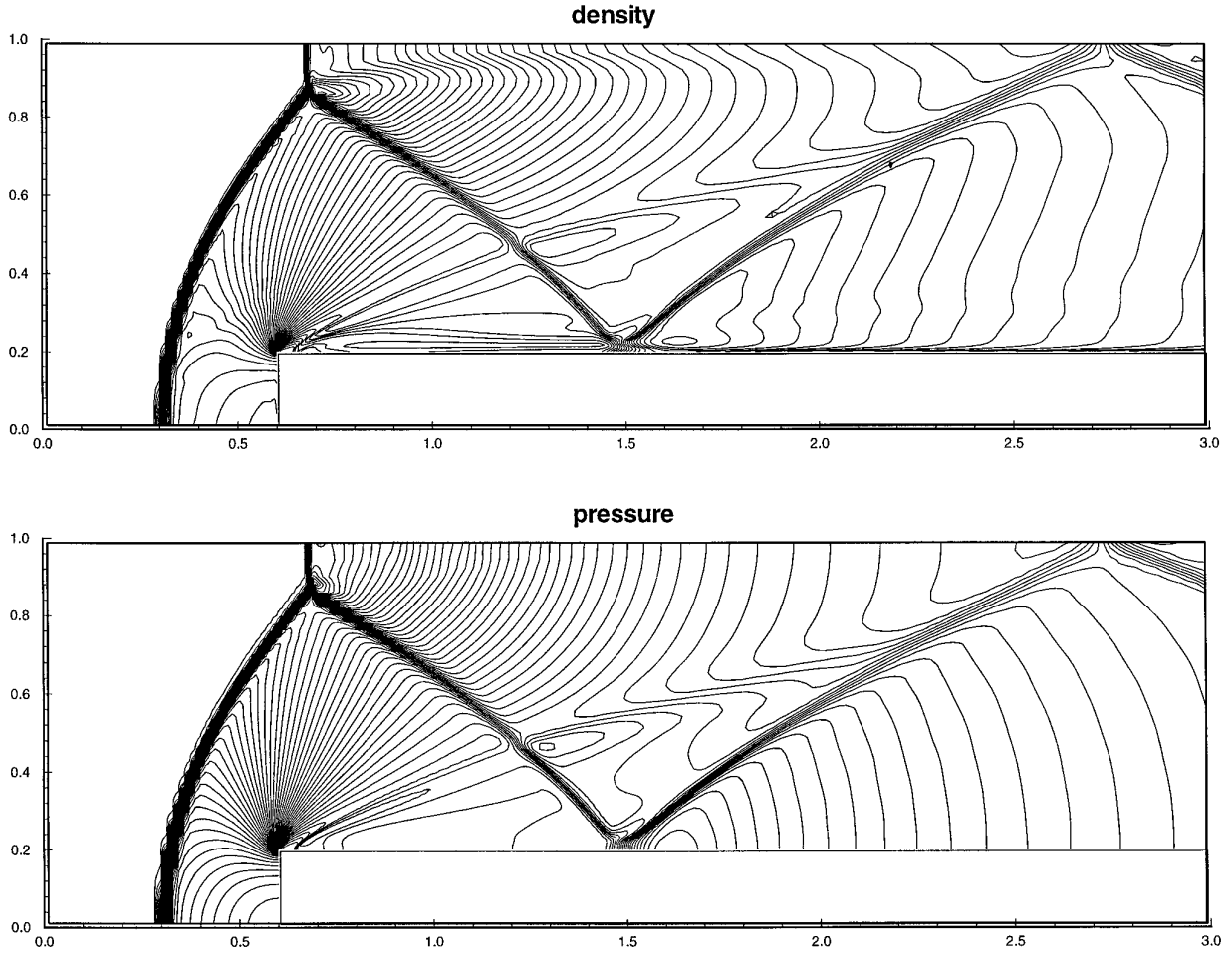

FIG. 7. Forward-facing step in a wind-tunnel—$M_\infty = 3.0$—second-order accurate results with EFMO; density and pressure contours.

to the upper wall again. Note also the presence of the contact discontinuity springing from the Mach intersection near the top wall on the density coutours. There is no separation bubble at the corner and no particular treatment is applied to avoid an entropy gradient downstream from the corner.

4. CONCLUDING REMARKS

A robust and low diffusive kinetic method has been proposed, combining the robustness of the original equilibrium flux method with the accuracy of the flux-difference splitting approach. The resulting EFMO numerical scheme, which requires the calculation of two intermediate states following the simple wave approach of Osher, exactly captures contact discontinuities and at the same time can withstand extreme conditions ranging from real vacuum apparition to very intense shock waves and rarefaction waves where regular FDS schemes fail in the absence of ad hoc fixes.

EFMO is particularly well suited for the numerical simulation of high-speed viscous flows where linear and nonlinear phenomenon are intimately associated and where a robust but diffusive FVS scheme cannot accurately resolve boundary layers and a low diffusive, but marginally stable, FDS scheme is subject to divergence or may produce unphysical results.

EFMO can be easily extended to include high-temperature real-gas effects by computing the intermediate states from an approximate Riemann problem with different values of γ for the left and right states. EFMO can also be used in an implicit method by explicitly evaluating the antidiffusive flux contribution and only impliciting the EFM fluxes as in a regular FVS approach.

APPENDIX

In this appendix detailed expressions for the EFMO numerical flux are given. The numerical flux for EFMO is defined by

$$F_{\mathrm{EFMO}}(U_L, U_R) = F_{\mathrm{EFM}}(U_L, U_R) + \Delta F, \tag{34}$$

where the EFM flux is defined by

$$F_{\mathrm{EFM}}(U_L, U_R) = F^+(U_L) + F^-(U_R) \tag{35}$$

and ΔF is the antidiffusive flux defined by

$$\Delta F = \begin{cases} -F^-(U_2) + F^-(U_1) & \text{if } v_n^* > 0 \\ +F^+(U_2) - F^+(U_1) & \text{otherwise.} \end{cases} \tag{36}$$

A.1. *Expression for EFM Fluxes*

At a given interface between left and right states U_L and U_R, the expression for F^+ and F^- associated with the EFM scheme are given in 3D by

$$F^{\pm} = \begin{pmatrix} fms = \rho(cD + v_n W) \\ fvn = v_n fms + pW \\ fvp = v_p fms \\ fvq = v_q fms \\ fen = fms\left[\dfrac{V^2}{2} + \dfrac{\gamma+1}{\gamma-1}\dfrac{c^2}{4}\right] + \frac{1}{2} p v_n W \end{pmatrix}, \tag{37}$$

where p, ρ, c are the pressure, density, and thermal speed, respectively ($c^2 = 2rT$), and v_n, v_p, v_q are the components of the velocity in a local system of axis in which v_n is the component normal to the interface. Additional definitions are given by

$$\begin{aligned} V^2 &= v_n^2 + v_p^2 + v_q^2 \\ D &= \pm \frac{1}{2\sqrt{\pi}} \exp(-s^2) \\ W &= \tfrac{1}{2}[1 \pm \mathrm{erf}(s)] \\ s &= v_n/c, \end{aligned} \tag{38}$$

where erf is the error function defined as

$$\mathrm{erf}(s) = \frac{2}{\sqrt{\pi}} \int_0^s \exp(-t^2)\, dt. \tag{39}$$

A.2. *Expression for Intermediate States*

Intermediate states U_1 and U_2 are completely defined by Eqs. (13)–(20). In the following, subscripts 1 and 2 denote intermediate states U_1 and U_2, respectively. First, the expression

$$A = a_L + a_R + \varepsilon \frac{\gamma - 1}{2}(v_{nL} - v_{nR}) \tag{40}$$

is computed, where $\varepsilon = \pm 1$ depending on the order chosen. If A is negative, we set

$$\Delta F = 0, \tag{41}$$

since this case corresponds to the vacuum apparition between states U_L and U_R. Another alternative could be to change the sign of ε if A is negative and proceed as shown below. In either case, the calculations

$$s_L = p_L/\rho_L^\gamma \tag{42}$$

$$s_R = p_R/\rho_R^\gamma \tag{43}$$

$$\rho_1 = \rho_L \left[\frac{A}{a_L\,(1 + (s_R/s_L)^{1/2\gamma})}\right]^{2/(\gamma-1)} \tag{44}$$

$$\rho_2 = \rho_1\,(s_L/s_R)^{1/\gamma} \tag{45}$$

$$p_1 = p_2 = p^* = s_L\rho_1^\gamma \tag{46}$$

$$a_1 = \sqrt{\gamma p_1/\rho_1} \tag{47}$$

$$v_n^* = v_{nL} - \frac{2\varepsilon}{\gamma - 1}\,(a_1 - a_L) \tag{48}$$

$$\begin{aligned} v_{n1} &= v_{n2} = v_n^* \\ v_{p1} &= v_{pL} \\ v_{p2} &= v_{pR} \\ v_{q1} &= v_{qL} \\ v_{q2} &= v_{qR} \end{aligned} \tag{49}$$

are performed which completely define U_1 and U_2.

ACKNOWLEDGMENTS

The present work was partly supported by the USA AFOSR Grant F49620-93-0332 and by the Direction de la Recherche et des Etudes Techniques of the French Ministry of Defense.

REFERENCES

1. D. I. Pullin, *J. Comput. Phys.* **34,** 231 (1980).
2. M. N. Macrossan, *J. Fluid Mech.* **266,** 69 (1994).
3. M. N. Macrossan, *J. Fluid Mech.* **217,** 167 (1990).
4. G. A. Bird, *Molecular Gas Dynamics and the Direct Simulation of Gas Flows* (Clarendon Press, Oxford, 1994).
5. J. C. Mandal and S. M. Deshpande, *Comput. Fluids* **23,** 447 (1994).
6. P. Villedieu and P. Mazet, *Rech. Aerosp.* **2,** 85 (1995).
7. M. N. Macrossan, *J. Comput. Phys.* **80,** 204 (1989).
8. M. N. Macrossan and R. I. Oliver, *Int. J. Numer. Methods Fluids* **17,** 177 (1993).
9. K. Xu, Ph.D. thesis, Columbia University, New York, 1993 (unpublished).
10. K. Xu and K. H. Prendergast, *J. Comput. Phys.* **109,** 53 (1993).
11. K. Xu and K. H. Prendergast, *J. Comput. Phys.* **114,** 9 (1994).
12. K. Xu, L. Martinelli, and A. Jameson, *J. Comput. Phys.* **120,** 48 (1995).
13. B. Van Leer, J. L. Thomas, P. L. Roe, and R. W. Newsome, AIAA Paper 87–1104 (unpublished).
14. D. Hänel and R. Schwane, AIAA Paper 89–0274 (unpublished).
15. B. Van Leer, NASA CP-3078, 1992 (unpublished).
16. M.-S. Liou and C. J. Steffen, High-order polynomial expansions (HOPE) for flux-vector splitting, NASA Tech. Memo. 104452, 1991 (unpublished).
17. M.-S. Liou and C. J. Steffen, *J. Comput. Phys.* **107,** 23 (1993).
18. R. Radespiel and N. Kroll, *J. Comput. Phys.* **121,** 66 (1995).
19. J. J. Quirk, *Int. J. Numer. Methods Fluids* **18,** 555 (1994).
20. H.-C. Lin, *J. Comput. Phys.* **117,** 20 (1995).
21. F. Coquel and M.-S. Liou, Stable and low diffusive hybrid upwind splitting methods, in *Computational Fluid Dynamics '92* (Elsevier, Amsterdam/New York, 1992).
22. D. Hänel, R. Schwane, and G. Seider, AIAA Paper 87–1105-CP (unpublished).
23. S. Osher and F. Solomon, *Math. of Comput.* **38,** 339 (1982).
24. T. W. Roberts, in *Numerical Methods for Fluid Dynamics 3*, edited by K. W. Morton and M. J. Baines (Clarendon, Oxford, 1988).
25. R. J. Hakkinen, I. Greber, L. Trilling, and S. S. Abarbanel, *NASA Memo 2-18-59W*, 1959 (unpublished).
26. B. Einfelt, C. D. Munz, P. L. Roe, and B. Sjögreen, *J. Comput. Phys.* **92,** 273 (1991).
27. P. R. Woodward and P. Colella, *J. Comput. Phys.* **54,** 115 (1984).
28. F. M. White, *Viscous Fluid Flow* (McGraw–Hill, New York, 1991).
29. R. W. MacCormack, *AIAA J.* **20,** 1275 (1982).
30. Z. Wang and B. E. Richards, *J. Comput. Phys.* **97,** 53 (1991).
31. J. J. Quirk, Ph.D. thesis, Cranfield University, Cranfield, 1991 (unpublished).
32. X. Zhong, *AIAA J.* **32,** 1606 (1994).
33. E. F. Toro, *Proceedings, 6th Int. Symposium on CFD, Vol. III, 1995* (unpublished).
34. A. Harten, P. D. Lax, and B. Van Leer, *SIAM Rev.* **25,** 33 (1983).
35. F. S. Billig, *J. Spac. Rockets* **4,** 822 (1967).
36. R. Menikoff, *SIAM J. Sci. Comput.* **15,** 1227 (1994).